American Mineralogist, Volume 93, pages 965–976, 2008

Rietveld structure refinement of $MgGeO_3$ post-perovskite phase to 1 Mbar

Atsushi Kubo,[1,*] Boris Kiefer,[2] Sang-Heon Shim,[3] Guoyin Shen,[4,†] Vitali B. Prakapenka,[4] and Thomas S. Duffy[1]

[1]Department of Geosciences, Princeton University, Princeton, New Jersey 08544, U.S.A.
[2]Department of Physics, New Mexico State University, Las Cruces, New Mexico 88003, U.S.A.
[3]Department of Earth, Atmospheric, and Planetary Sciences, Massachusetts Institute of Technology, Cambridge, Massachusetts 02319, U.S.A.
[4]Center for Advanced Radiation Sources, University of Chicago, Chicago, Illinois 60637, U.S.A.

Abstract

Using the $CaIrO_3$-type structure model (space group *Cmcm*), lattice parameters and atomic positions of the $MgGeO_3$ post-perovskite (pPv) phase were determined based on Rietveld refinements at 78–109 GPa and first-principles calculations based on density functional theory. The reproducibility of structural parameters obtained for different samples, consistency with theoretical calculations, and good agreement with expected bond lengths based on structurally similar materials all provide evidence for both validity of $CaIrO_3$-type structure model for the pPv phase in $MgGeO_3$ exceeding 1 Mbar and reliability of structural parameters obtained by Rietveld refinements approaching 1 Mbar. The $MgGeO_3$ pPv phase exhibits strong anisotropy in axial compressibility, with the **b**-axis being most compressible. The polyhedral bulk modulus for the GeO_6 octahedron is 1.9× larger than that for the MgO_8 hendecahedron. Examination of neighboring O-O distances shows that the O-O distance aligned along the **a** direction is one of the longest and that aligned along **c** is one of the shortest, and these may be related to the lower compressibility along **c** compared with **a**. Comparison of structural features of $MgGeO_3$ pPv with those for $MgSiO_3$, $NaMgF_3$, and $CaIrO_3$ pPv show that $MgSiO_3$ pPv has more similarity with $NaMgF_3$ and $MgGeO_3$ pPv than with $CaIrO_3$ pPv in such parameters as degree of octahedral distortion, implying that both $NaMgF_3$ and $MgGeO_3$ pPv are better analogs to $MgSiO_3$ pPv than $CaIrO_3$ pPv.

Keywords: Post-perovskite, $MgGeO_3$, Rietveld refinement, high-pressure experiment, first-principles calculation, laser-heated diamond anvil cell, density functional theory, polycrystalline X-ray diffraction

Introduction

The post-perovskite (pPv) phase, with $CaIrO_3$-type structure (space group *Cmcm*) (Rodi and Babel 1965) (Fig. 1) discovered in $MgSiO_3$ at 125 GPa and 2500 K (Murakami et al. 2004; Oganov and Ono 2004; Iitaka et al. 2004), has been extensively studied due to its geophysical importance (e.g., Ono and Oganov 2006; Hirose 2006; Merkel et al. 2007). Due to the experimental difficulties in the synthesis of silicate pPv phase at >1 Mbar and high temperature (e.g., Shim et al. 2004; Mao et al. 2004; Shieh et al. 2006), theoretical calculations have played an important role in predicting stability and physical properties of the pPv phase (e.g., Oganov and Ono 2004; Tsuchiya et al. 2004; Oganov et al. 2005; Wentzcovitch et al. 2006). Experimental studies have also focused on the $CaIrO_3$-type pPv phase in analog materials to silicates such as $MgGeO_3$ (Hirose et al. 2005; Kubo et al. 2006), $MnGeO_3$ (Tateno et al. 2006), and $NaMgF_3$ (Liu et al. 2005; Martin et al. 2006a). For example, $MgGeO_3$ pPv phase can be synthesized as low as ~70 GPa at 2000 K (Hirose et al. 2005; Runge et al. 2006), and the pPv phase of $CaIrO_3$ is stable at ambient conditions up to ~1650 K (Hirose and Fujita 2005; Kojitani et al. 2007). By using these analog materials, predictions for the behavior of the silicate pPv phase can be obtained experimentally (e.g., Merkel et al. 2006; Miyagi et al. 2008; Shim et al. 2007; Walte et al. 2007). It should also be noted that the $CaIrO_3$-type phase also has been discovered in several sesquioxide compounds at high pressures: Al_2O_3 (Ono et al. 2006a), Fe_2O_3 (Ono and Ohishi 2005), and Mn_2O_3 (Santillán et al. 2006).

At high pressures where single-crystal diffraction is not accessible, the Rietveld method has been applied to examine detailed structures of polycrystalline materials (e.g., Fiquet et al. 2002). As pressure increases, the use of this technique becomes more challenging because diffraction data may suffer from effects of differential stress, preferred orientation, and poorer crystal statistics. Although differential stress in the sample can be reduced by annealing (e.g., Fiquet et al. 2002), it is generally difficult to eliminate preferred orientation in the sample. If preferred orientation exists in the sample, refined parameters that depend on diffraction intensities such as atomic positions could be affected (Martin et al. 2006b), even if lattice parameters can be reliably refined. Theoretical calculations based on density functional theory also can predict structure parameters as a function of pres-

* Present address: Center for Advanced Radiation Sources, University of Chicago, Chicago, Illinois 60637, U.S.A. E-mail: akubo@cars.uchicago.edu
† Present address: High Pressure Collaborative Access Team, Carnegie Institution of Washington, Argonne National Laboratory, Argonne, Illinois 60439, U.S.A.

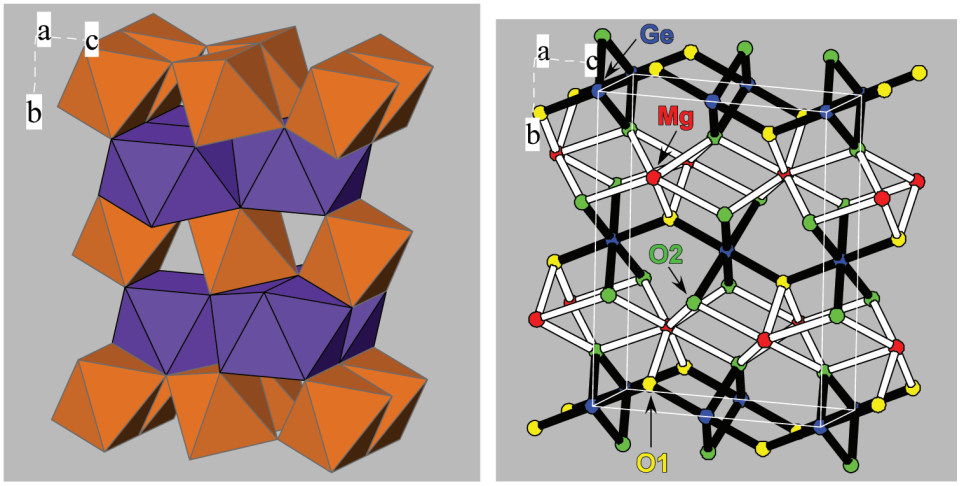

FIGURE 1. Crystal structure of $CaIrO_3$-type post-perovskite phase in $MgGeO_3$. (**a**) MgO_8 and GeO_6 polyhedra are shown with blue and orange, respectively. (**b**) Spheres show atoms: red = Mg; blue = Ge; yellow = O1 (corner-shared oxygen); green = O2 (edge-shared oxygen). White and black bars indicate Mg-O and Ge-O bonds, respectively.

sure (e.g., Kubo et al. 2006). Due to the complementary nature of these two methods, use of both Rietveld and theory is desirable to obtain robust structure parameters at very high pressures.

So far, the Rietveld method has been applied to the pPv phase in $MgGeO_3$ (Hirose et al. 2005, Kubo et al. 2006), Fe_2O_3 (Ono and Ohishi 2005), $MnGeO_3$ (Tateno et al. 2006), Mn_2O_3 (Santillán et al. 2006), and $NaMgF_3$ (Martin et al. 2006a) mainly to confirm that diffraction data are consistent with the $CaIrO_3$-type structure. An important goal of our study is to provide a test of the reliability of Rietveld refinement methods at megabar pressures where effects such as poor crystal statistics, limited 2θ range, preferred orientation, and differential stress may limit refinement quality. Here we examine pressure and temperature dependencies of structure parameters of the pPv phase in $MgGeO_3$ by conducting both Rietveld refinements and first-principles calculations. The results are compared with structure parameters predicted for $MgSiO_3$ pPv at 120 GPa, $NaMgF_3$ pPv at 30 GPa, and experimentally determined for $CaIrO_3$ pPv at ambient conditions. This study presents further analysis of data reported by Kubo et al. (2006).

METHODS

High-pressure experiments

The pPv phase was synthesized from $MgGeO_3$ orthopyroxene using laser-heated diamond cells. Powder X-ray diffraction of the starting material showed orthoenstatite with minor amounts of excess GeO_2, as reported in Kubo et al. (2006). Unit-cell parameters of the orthopyroxene at ambient conditions were determined to be a = 18.8088(9) Å, b = 8.9490(4) Å, and c = 5.3431(2) Å from Le Bail refinement. These unit-cell parameters are in very good agreement with Ozima and Akimoto (1983). This starting material was mixed with 20 wt% Pt powder that served as both a pressure standard and laser absorber. Experiments were conducted using either Ar (run 1) or NaCl (run 2) as pressure media and thermal insulation. The sample was heated using a Nd:YLF laser (TEM_{00} mode) with double-sided heating (Shen et al. 2001).

Angle dispersive X-ray diffraction experiments were conducted at beamline 13-ID-D of the GSECARS sector at the Advanced Photon Source (APS) (Shen et al. 2005). The incident monochromatic X-ray beam of 0.3344 Å wavelength was focused to a size of ~6 × 6 μm^2. An angle dispersive geometry with an image plate (Mar 345) was used. The detector was calibrated using CeO_2. Pressure was determined from the equation of state of platinum (Holmes et al. 1989). Further details can be found in Kubo et al. (2006).

In run 1, the pPv phase was synthesized by heating the starting material to 1600–1900 K at 83–87 GPa for 10 min. We then compressed the sample to 99 GPa at room temperature and heated to ~1600 K. After quenching to room temperature, we further compressed the sample to 109 GPa at room temperature, but diffraction peaks of Pt and Ar completely overlapped at this pressure. The sample was then decompressed without further heating. Diffraction data were collected at room temperature at various pressures during both compression and decompression. In run 2, $MgGeO_3$ pPv phase was synthesized during laser heating at 92–94 GPa and 1400–1700 K. Diffraction data were also collected in situ during laser heating. Subsequently, the sample was decompressed without heating, and diffraction data were obtained at various pressures.

Rietveld refinements

Two-dimensional (2D) diffraction images obtained after laser heating contained continuous Debye rings from all phases in the diamond cell, and few diffraction spots were present (Fig. 2). These two factors are essential to conduct reliable Rietveld refinement (cf. McCusker et al. 1999). To reduce the intensity of some strong diffraction spots originating from diamond in run 2, we tilted the diamond cell 1° away from the normal. For this reason, the outermost Debye rings were only partially recorded. To obtain one-dimensional (1D) data with the maximum 2θ range and reliable intensities, we restricted the region of integration to a ~60° slice where the outermost Debye ring was recorded (Fig. 2). Most of the observable diffraction spots in this region were masked, and then using Fit2d (Hammersley et al. 1996), the 2D data were integrated to obtain 1D diffraction patterns that were used for the Rietveld refinements.

We estimated the standard deviation (σ) of diffraction intensity at each 2θ based on the equation (Von Dreele, unpubl.): $\sigma = (F\sqrt{I})/\tan 2\theta$, where F is the parameter that represents intrinsic noise level of each diffraction datum and I is the diffraction intensity including background. F was assumed to be constant across the 2θ range for each pattern. To determine F, we sampled the noise level (σ) and background intensity I at 2θ = 5.2 ± 0.4° where no diffraction peaks were observed.

Prior to Rietveld refinements, we conducted Le Bail refinements using GSAS/EXPGUI (Larson and Von Dreele 2004; Toby 2001) to refine lattice parameters and peak shape parameters (profile terms "GW and LX" in the constant wavelength profile function 2 in GSAS) to be used as initial values in Rietveld refinement. Here GW and LX are the basic profile terms that define pseudo-Voigt peak shape. It is known empirically that Le Bail refinement yields the best fitting results (with best reliability factor) achievable in Rietveld refinement. This in turn means that the diffraction data that cannot be well fitted by Le Bail refinement are unlikely to be successfully refined by Rietveld refinement.

After successful Le Bail refinement, we conducted Rietveld refinement using GSAS/EXPGUI by the following three steps. For each step, parameters for the pPv phase, Pt, and either Ar or NaCl were separately refined initially, but eventually refined simultaneously. Before starting the refinement, a background was manually defined using a Chebyshev polynomial (typically 10 terms). In the first step, we refined only phase fractions and atomic positions assuming no preferred orientation, with lattice parameters and profile terms being fixed. Subsequently, we fixed all the parameters refined in the first step, and then refined only spherical harmonic terms for preferred orientation correction. We assumed cylindrical

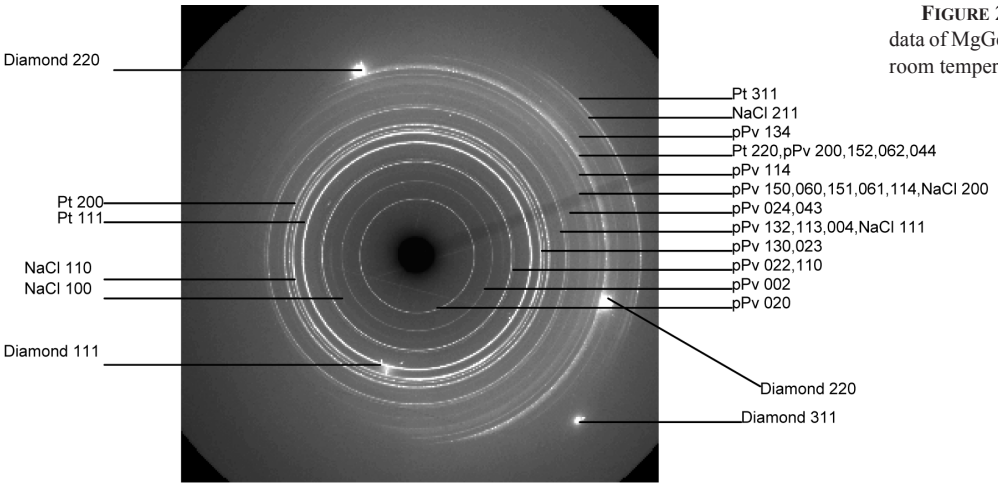

FIGURE 2. Polycrystalline diffraction data of $MgGeO_3$ pPv phase at 88 GPa and room temperature from run 2 (B019).

sample symmetry (fiber texture). The spherical harmonic order used for refinements was 2 (run 1) or 4 (run 2) for the pPv phase, and 6 for Pt, NaCl, and Ar. In the third step, we refined all the parameters including lattice parameters and profile terms simultaneously to complete the refinement and to obtain correct estimated standard deviations σ (McCusker et al. 1999). For data obtained at 105 and 109 GPa in run 1, we ignored the presence of Ar in the diffraction data because peak overlap between Pt and Ar was nearly complete and diffraction peaks from Ar seemed weak and broad.

It is very challenging to refine isotropic displacement parameter U_{iso} [$=B/(8\pi^2)$, where B is Debye parameter] from diffraction data obtained under pressure with a limited 2θ range. We concluded that our diffraction data do not have enough quality to refine displacement parameters because negative displacement parameters that are physically meaningless were typically obtained. Sugahara et al. (2006) demonstrated in a single-crystal X-ray diffraction study up to 15 GPa that equivalent isotropic displacement parameters B_{iso} for perovskite-type $MgSiO_3$ do not change strongly as a function of pressure at room temperature. Therefore, we fixed U_{iso} to the following values: 0.005 Å^2 for all atoms in the pPv phase, 0.004 Å^2 for Pt, 0.04 Å^2 for Ar, and 0.02 Å^2 for all atoms in B2 phase of NaCl. These U_{iso} values are based on equivalent isotropic displacement parameters of $MgSiO_3$ perovskite (Sugahara et al. 2006) and Debye parameters listed in *International Tables for X-ray Crystallography* (Ibers et al. 1968) for Pt (293 K), krypton (93 K), and B1 phase of NaCl (293 K), respectively.

We tried to reduce the number of refined parameters as much as possible to avoid mathematically better but physically meaningless fitting ("overfitting"). For this purpose, we did not refine the background and U_{iso}, and we limited the number of peak shape parameters and spherical harmonic order for the preferred orientation correction to be as small as possible. In fact, Kubo et al. (2006) presented atomic positions for $MgGeO_3$ pPv phase with some differences from those reported here because more parameters were refined for each phase including U_{iso} and one more Gaussian-related peak shape parameter in that study. The atomic positions reported by Kubo et al. (2006) are superseded by those obtained here.

Theoretical calculations

We carried out first-principles calculations based on density functional theory (Hohenberg and Kohn 1964) to calculate atomic positions and lattice parameters of the pPv phase as a function of pressure at 0 K as described in Kubo et al. (2006). These calculations were carried out with the software package VASP (Kresse and Hafner 1993, 1994; Kresse and Furthmüller 1996) using the projector-augmented-wave (PAW) method (Blöchl 1994; Kresse and Joubert 1999). Electronic correlations were treated within the local density approximation (LDA) in the parameterization of Perdew and Zunger (1981). The reliability of the predicted structure was verified by alternate calculations within the general gradient approximation (GGA) in the parameterization by Perdew-Burke-and Ernzerhof (PBE, Perdew et al. 1996). We used PAW-LDA potentials with core region cut-off radii of 2.0 a.u. for Mg (valence configuration $2p^63s^2$), 1.9 a.u. for Ge (valence configuration $3d^{10}4s^24p^2$), and 1.52 a.u. for O (valence configuration $2s^22p^4$). The core cut-off radii and valence configurations in the PAW-PBE calculations were the same with the exception of the cut-off radius for Ge that was 2.3 a.u. Tests showed that converged solutions to the Kohn-Sham equations (Kohn and Sham 1965) could be obtained with an energy-cutoff of 600 eV and a $6 \times 4 \times 6$ k-point grid. Total energies are converged to better than 2.3 meV/atom, and stresses due to the incompleteness of the basis-set are <0.5 GPa and 0.6 GPa in the LDA and GGA calculations, respectively.

We optimized the lattice parameters and atomic positions in the $CaIrO_3$-type structure for volumes between 108 and 180 Å^3 by LDA and between 110 and 195 Å^3 by GGA to determine the groundstate of $MgGeO_3$ at these volumes. The pressure and all structural parameters of $MgGeO_3$ pPv were obtained from the relaxed configurations for eleven volumes in the pressure range of –2 to 298 GPa by LDA and twelve volumes between –4 and 298 GPa by GGA. It is noted that the pPv phase is metastable below ~47 GPa at 0 K according to the pPv phase transition boundary determined by Hirose et al. (2005), and Kubo et al. (2006) have confirmed the stability of the pPv phase up to 2 Mbar at ~1600 K. The results are shown in Table 1.

RESULTS AND DISCUSSION

Using the $CaIrO_3$-type structure model, we could successfully conduct Rietveld refinements for three diffraction spectra in run 1 in the pressure range of 100–109 GPa and seven diffraction patterns including two data at high temperatures in run 2 at 78–94 GPa. Although we had diffraction data in a wide pressure range down to 7 GPa, we could not successfully refine lower pressure data probably due to higher differential stresses and metastability of the pPv phase at pressures < ~45 GPa (Kubo et al. 2006). Peak widths for diffraction data below 45 GPa are much broader than higher pressure data. Figure 3 shows a selected Rietveld refinement result (see online supplementary materials[1] for complete Rietveld results). It is clear from Figure 3 that diffraction peaks of the pPv phase are well fitted. Together with the reasonable atomic positions and lattice parameters listed in Table 2, this observation validates the $CaIrO_3$-type structure model for the pPv phase in $MgGeO_3$ at 78–109 GPa. However, misfit can be

[1] Deposit item AM-08-032, Supplementary Table 1 and Supplementary Figures 1 and 2 (complete Rietveld results). Deposit items are available two ways: For a paper copy contact the Business Office of the Mineralogical Society of America (see inside front cover of recent issue) for price information. For an electronic copy visit the MSA web site at http://www.minsocam.org, go to the American Mineralogist Contents, find the table of contents for the specific volume/issue wanted, and then click on the deposit link there.

TABLE 1. Lattice parameters and atomic positions for $MgGeO_3$ post-perovskite phase at 0 K predicted by theoretical calculations using local density approximation (LDA) and generalized gradient approximation (GGA)

						LDA					
P (GPa)	−2.0	−0.1	3.6	27.5	46.5	68.1	86.3	108.5	148.6	196.9	297.9
a (Å)	2.8047	2.7960	2.7815	2.7060	2.6625	2.6228	2.5943	2.5642	2.5194	2.4760	2.4082
b (Å)	9.3034	9.2644	9.2008	8.8729	8.6843	8.5093	8.3856	8.2543	8.0581	7.8659	7.5527
c (Å)	6.8984	6.8754	6.8382	6.6515	6.5471	6.4521	6.3853	6.3150	6.2105	6.1100	5.9543
Mg *y*	0.2595	0.2590	0.2580	0.2547	0.2534	0.2525	0.2519	0.2514	0.2507	0.2502	0.2494
O1 *y*	0.9161	0.9161	0.9159	0.9155	0.9153	0.9152	0.9151	0.9150	0.9150	0.9150	0.9153
O2 *y*	0.6322	0.6326	0.6333	0.6368	0.6387	0.6404	0.6416	0.6428	0.6445	0.6461	0.6487
O2 *z*	0.4401	0.4399	0.4394	0.4379	0.4372	0.4366	0.4362	0.4358	0.4353	0.4348	0.4340

						GGA						
P (GPa)	−4.1	0.0	9.6	15.8	42.0	62.3	85.3	104.5	127.9	169.6	219.5	298.1
a (Å)	2.8738	2.8504	2.8065	2.7830	2.7075	2.6640	2.6239	2.5954	2.5655	2.5210	2.4780	2.4248
b (Å)	9.5774	9.4768	9.2879	9.1877	8.8643	8.6768	8.5049	8.3827	8.2521	8.0555	7.8629	7.6158
c (Å)	7.0849	7.0214	6.9054	6.8442	6.6542	6.5490	6.4527	6.3847	6.3135	6.2086	6.1076	5.9837
Mg *y*	0.2629	0.2610	0.2581	0.2570	0.2541	0.2530	0.2523	0.2519	0.2515	0.2509	0.2505	0.2500
O1 *y*	0.9162	0.9160	0.9158	0.9158	0.9157	0.9156	0.9157	0.9157	0.9158	0.9159	0.9162	0.9166
O2 *y*	0.6302	0.6313	0.6333	0.6344	0.6376	0.6393	0.6409	0.6419	0.6431	0.6447	0.6462	0.6480
O2 *z*	0.4414	0.4406	0.4394	0.4389	0.4377	0.4371	0.4366	0.4363	0.4360	0.4355	0.4351	0.4345

TABLE 2. Lattice parameters and atomic positions for $MgGeO_3$ pPv phase determined by Rietveld refinements

Rietveld data	A036	A038	A042	B017	B018	B019	B020	B038	B040	B041
P (GPa)	105.4	109.3	100.2	92.1	93.6	87.8	89.5	85.0	79.2	78.2
T (K)	300	300	300	1740	1420	300	300	300	300	300
a (Å)	2.5718(8)	2.5677(7)	2.5811(5)	2.6001(3)	2.5987(4)	2.5971(4)	2.5949(3)	2.6018(4)	2.6113(4)	2.6127(4)
b (Å)	8.3274(21)	8.3132(19)	8.3628(14)	8.4123(9)	8.4107(11)	8.4089(9)	8.4009(9)	8.4259(11)	8.4602(12)	8.4674(12)
c (Å)	6.3536(11)	6.3453(15)	6.3730(10)	6.4099(7)	6.4079(8)	6.4064(7)	6.4013(6)	6.4161(7)	6.4381(7)	6.4413(8)
Mg *y*	0.2601(21)	0.2573(19)	0.2570(14)	0.2614(13)	0.2590(14)	0.2533(10)	0.2568(11)	0.2573(12)	0.2555(12)	0.2563(12)
O1 *y*	0.9061(38)	0.9117(34)	0.9081(25)	0.9101(29)	0.9083(34)	0.9176(24)	0.9138(25)	0.9127(27)	0.9121(27)	0.9139(28)
O2 *y*	0.6404(23)	0.6410(21)	0.6383(16)	0.6432(13)	0.6412(15)	0.6400(12)	0.6412(12)	0.6398(13)	0.6367(14)	0.6372(15)
O2 *z*	0.4365(35)	0.4365(35)	0.4319(24)	0.4417(18)	0.4365(20)	0.4395(17)	0.4375(16)	0.4375(17)	0.4370(17)	0.4377(18)
R_{wp} (%)	3.1	2.8	2.2	2.9	3.3	3.4	3.1	3.5	3.3	3.5

Note: R_{wp} shows the quality of the least squares refinement after background subtraction based on following residual function: $R_{wp} = [\sum w(I_o - I_c)^2/\sum wI_o^2]^{1/2}$, where w, I_o, and I_c are weight, observed intensity, and calculated intensity, respectively (Larson and Von Dreele 2004).

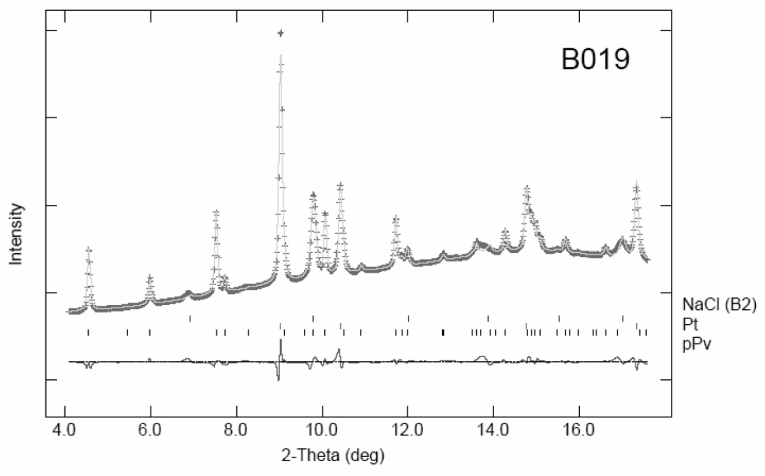

FIGURE 3. An example of Rietveld refinement result at 88 GPa and room temperature from run 2. The crosses represent observed intensities (I_{obs}). The solid line is the calculated intensities (I_{calc}). The tick marks show the positions of calculated diffraction lines: upper ticks = NaCl (B2-phase); middle ticks = Pt; lower ticks = pPv. The line below the tick marks is the intensity difference curve ($I_{obs} - I_{calc}$).

seen for the most intense diffraction peak of Pt 200 and peaks from B2 phase of NaCl due to differential stress in the sample chamber, as discussed later. To evaluate the effect of misfit of Pt on refined atomic positions of the pPv phase, we conducted another set of Rietveld refinements using the diffraction data with the Pt 200 peak manually subtracted. In these refinements, the atomic positions were mostly reproduced within 1σ deviation from original results, implying that effects of differential stress in Pt are not significant within 1σ. However, for patterns A038 and A042 (Table 2 and online supplementary items[1]), atomic positions were not reproducible within 3σ. Therefore, despite better *R*-factor in run 1 than in run 2 (Table 2), Rietveld results from run 2 appear to be more reliable than those from run 1, which is supported by the larger 2θ range, weaker Pt intensity, and less peak overlap of Pt with pressure medium in run 2 (cf. Toby 2006). Note that the uncertainty shown in Table 2 and all the figures in this paper are 1σ obtained from least squares calculations in Rietveld refinements, and this represents the precision of the recovered parameters.

Lattice parameters, axial ratios, and unit-cell volumes

Lattice parameters, axial ratios, and unit-cell volume of the pPv phase determined in this study are listed in Tables 1 and 2. These results are also shown in Figure 4 together with Rietveld

results by Hirose et al. (2005) for $MgGeO_3$ pPv at 78 GPa and room temperature, theoretical predictions for $MgSiO_3$ pPv at 120 GPa and 0 K by Tsuchiya et al. (2004) and $NaMgF_3$ pPv at 30 GPa and 0 K by Umemoto et al. (2006), and single-crystal X-ray diffraction results for $CaIrO_3$ at ambient conditions by Rodi and Babel (1965). Note that theoretical results for $MgSiO_3$ pPv by Tsuchiya et al. (2004) and Iitaka et al. (2004) using LDA are similar to within 0.2% for atomic positions and 0.3% for lattice parameters, and the differences between theoretical results by GGA (Oganov and Ono 2004) and LDA (Tsuchiya et al. 2004; Iitaka et al. 2004) are within 0.2% for atomic positions and 0.9% for lattice parameters. Although Rietveld results are available for both $MgSiO_3$ pPv (Ono et al. 2006b) and $NaMgF_3$ pPv (Martin et al. 2006a), we use theoretical results for these phases because, unlike for $MgGeO_3$, theory and experiment are not currently in good agreement in terms of atomic positions. In this and subsequent figures, open symbols refer to data at room temperature (Rietveld) or 0 K (theory), and filled symbols indicate high-temperature data. Also, in the following discussion, we compare structure parameters in $MgGeO_3$ at ~70 GPa with those in $MgSiO_3$, $NaMgF_3$, and $CaIrO_3$ pPv phases at 120, 30, and 0 GPa, respectively, as these pressures are close to lowest stability limit of these pPv phases at high temperatures.

Almost all the data points at room temperature in Figure 4a determined here by Rietveld refinement fall on the compression curves previously reported by Kubo et al. (2006) that were based on individual peak fitting using five diffraction peaks of the pPv phase, indicating that peak fitting can yield lattice parameters that are as reliable as those determined by Rietveld method. Lattice parameters predicted by LDA (GGA) are slightly smaller (larger) than those observed in our experiments, which are typical for these calculations.

Figure 4b shows ratios of unit-cell axes. Pressure dependence of *b*/*a* ratio shows that the **b**-axis is more compressible than **a-** and **c**-axes whose axial compressibilities are similar as manifested by less pressure dependence of *c*/*a* ratio. This finding is consistent with experimental observations for the $MgGeO_3$ pPv phase (Hirose et al. 2005; Merkel et al. 2006; Kubo et al. 2006) and the $MgSiO_3$ pPv phase (e.g., Murakami et al. 2004). While theory predicts a comparatively strong pressure dependence of *b*/*a*, experimental results show a small pressure dependence at 80–110 GPa, which is also reported in Kubo et al. (2006). On the other hand, *c*/*a* at 80–110 GPa shows a mild increase with pressure, in excellent agreement between experiments and theory. At 1700 K, both *b*/*a* and *c*/*a* become slightly smaller. The *b*/*a* ratio of $MgSiO_3$ pPv is expected to be 0.8, 4.2, and 4.2% larger than

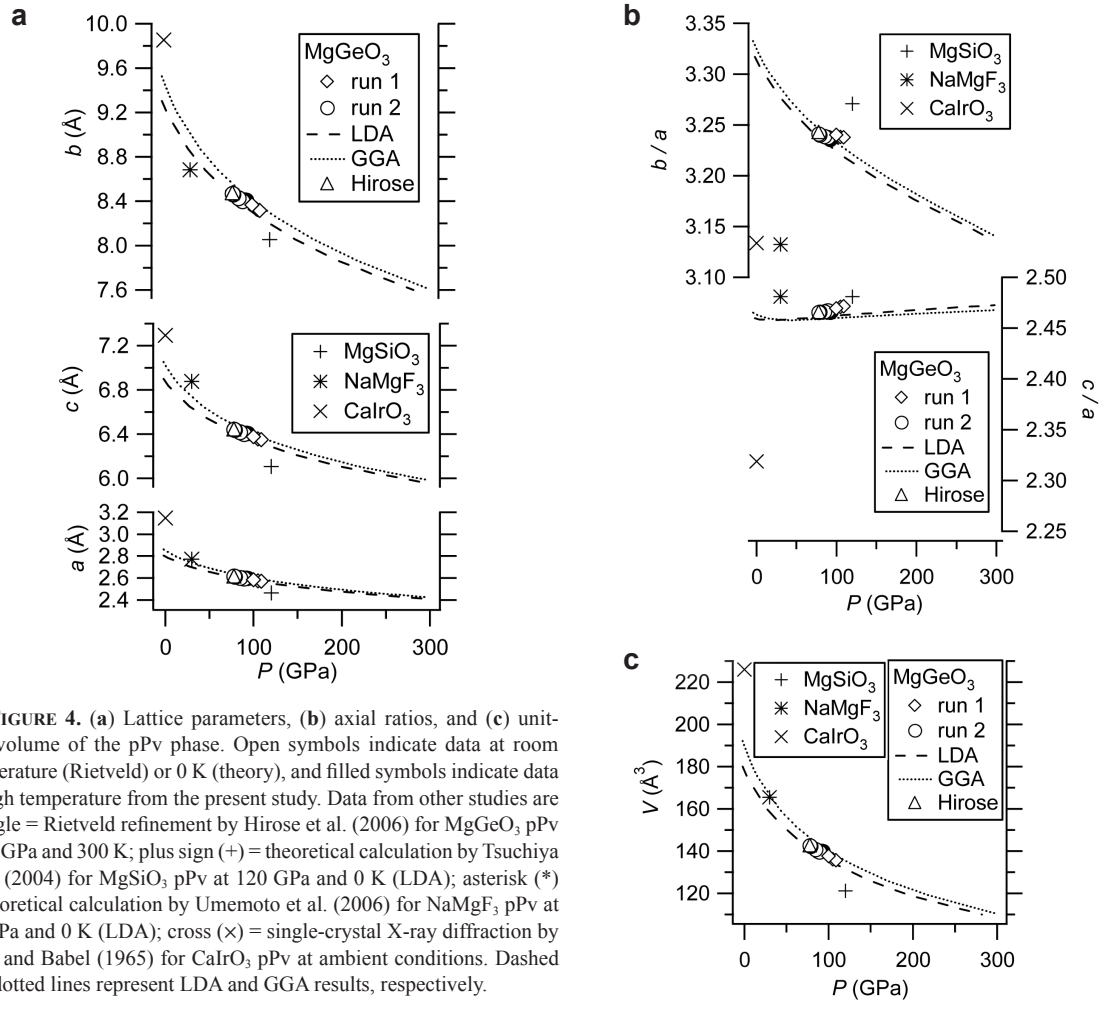

FIGURE 4. (**a**) Lattice parameters, (**b**) axial ratios, and (**c**) unit-cell volume of the pPv phase. Open symbols indicate data at room temperature (Rietveld) or 0 K (theory), and filled symbols indicate data at high temperature from the present study. Data from other studies are triangle = Rietveld refinement by Hirose et al. (2006) for $MgGeO_3$ pPv at 78 GPa and 300 K; plus sign (+) = theoretical calculation by Tsuchiya et al. (2004) for $MgSiO_3$ pPv at 120 GPa and 0 K (LDA); asterisk (*) = theoretical calculation by Umemoto et al. (2006) for $NaMgF_3$ pPv at 30 GPa and 0 K (LDA); cross (×) = single-crystal X-ray diffraction by Rodi and Babel (1965) for $CaIrO_3$ pPv at ambient conditions. Dashed and dotted lines represent LDA and GGA results, respectively.

that of $MgGeO_3$, $NaMgF_3$, and $CaIrO_3$ pPv phases, respectively, while the c/a ratio of $MgSiO_3$ pPv is 0.8, 0, and 6.5% larger than that of $MgGeO_3$, $NaMgF_3$, and $CaIrO_3$ pPv phases, respectively, showing remarkable similarity of $MgGeO_3$ pPv with $MgSiO_3$ pPv in terms of axial ratios.

Figure 4c shows unit-cell volumes determined by Rietveld refinement and theory. All data points determined by Rietveld refinement fall on the compression curve of the pPv phase experimentally determined by Kubo et al. (2006), again validating consistency between peak fitting and Rietveld methods. It is noted that a previous Rietveld refinement by Hirose et al. (2005) is also in excellent agreement with our Rietveld results in spite of serious inconsistency in atomic positions between our results and Hirose et al. (2005) as discussed later. By using a third-order Birch-Murnaghan equation of state, LDA results give zero-pressure isothermal bulk modulus (K_0) of 205 GPa with pressure derivative (K_0') of 4.28, while GGA results yield K_0 of 174 GPa with K_0' of 4.25. Our GGA results agree well with theoretical work by Fang and Ahuja (2006) using GGA. Since LDA results are more consistent with experimentally determined K_0 of 207(5) GPa and K_0' of 4.4 by Kubo et al. (2006), we mainly use LDA results for comparison with Rietveld results hereafter.

Preferred orientation and differential stress

Figure 5a shows values of texture indices from the Rietveld refinements, parameters that indicate the magnitude of preferred orientation, with $J = 1$ if there is no preferred orientation, otherwise $J > 1$ and $J = \infty$ for a single crystal (Von Dreele 1997). All materials in the sample chamber exhibit evidence for preferred orientation. In all diffraction patterns, the relative intensity of pPv diffraction peaks 020 and 110 are stronger and weaker than expected from the ideal intensity relationship, respectively. All the spherical harmonic coefficients for the pPv phase are shown in Supplementary Table 1[1], from which one can obtain pole figures. Our pole figure analysis showed that the **b**-axis tends to align perpendicular to the compression direction of the diamond cell while {100}, {110}, {101}, and {111} tend to align almost parallel to the compression axis. These observations are consistent with preferred orientation of $MgGeO_3$ pPv observed by Merkel et al. (2006) and theoretical predictions by Oganov et al. (2005) for $MgSiO_3$ pPv. Similar experimental observations have been reported for both $MgSiO_3$ and Mn_2O_3 pPv by Murakami et al. (2004) and Santillán et al. (2006), respectively.

We estimated differential stress in Pt from d-values of Pt111 and Pt200 based on Singh's (1993) method, assuming an axially symmetric stress field in the sample, iso-stress model (Reuss limit), and elastic anisotropy of Pt (Kavner and Duffy 2003). Details of our calculations can be found in Runge et al. (2006). The results, shown in Figure 5b, indicate that the magnitude of differential stress in our samples ($MgGeO_3$ mixed with Pt) is ~0.3–1.0 GPa. There is no discernible correlation between the magnitude of differential stress and type of pressure medium (Ar or NaCl). At high temperature, differential stress tends to be somewhat reduced.

Atomic positions

There are four variable atomic positions (fractional coordinates) in the $CaIrO_3$-type structure (Fig. 1). In the present study, we represent atomic positions of the ABX_3 pPv phase as follows; A (0, y, 1/4), B (0, 0, 0), X1 (0, y, 1/4), X2 (0, y, z), where X1 and X2 correspond to corner and edge shared anions of the BX_6 octahedron (Fig. 1), respectively. Note that Rodi and Babel (1965) contains typographical errors in the table of atomic positions for $CaIrO_3$.

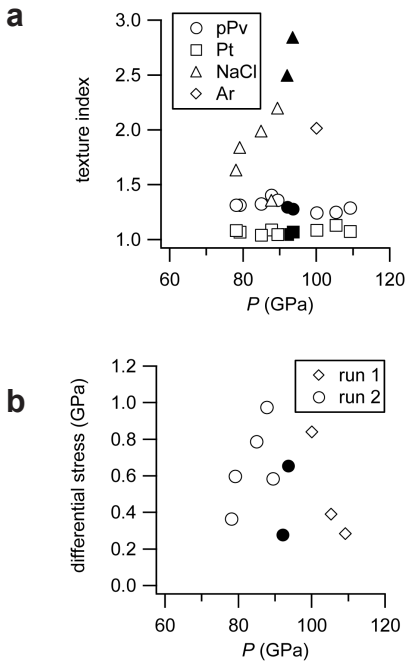

FIGURE 5. (**a**) Texture index obtained from Rietveld refinements. (**b**) Differential stress in Pt estimated from 111 and 200 diffraction peaks.

Atomic positions from this study are shown in Tables 1–2, and Figure 6. Results by LDA and GGA calculations are in good agreement. Rietveld results are consistent with theoretical results within 3σ, although both considerable data scatter and the limited pressure range make it difficult to constrain the pressure dependence of atomic positions solely from Rietveld results. Our theoretical calculations predict small changes of the atomic positions at pressures between ~50 and 300 GPa, implying no change in compression mechanism of the pPv phase at this pressure range. However, Mg y and O2 positions change much more between 0 and ~50 GPa, implying different compression behavior in the low-pressure metastable region. Within an uncertainty of 3σ, we do not find any consistent temperature dependence of the atomic positions from Rietveld results, and thermal effects may be below our level of resolution.

Hirose et al. (2005) reported Rietveld refinement from a single diffraction spectrum of $MgGeO_3$ pPv at 78 GPa and 300 K. Hirose et al.'s results for Mg y and O2 z are consistent with our results, but their results for O1 y and O2 y are quite inconsistent beyond 3σ. The diffraction data obtained by Hirose et al. (2005) exhibits a markedly different intensity relationship compared with our data in Figure 3. According to our Rietveld refinement, the texture index of the pPv phase is always <1.5 (Fig. 5a), showing that preferred orientation of our samples is minimal. Also, our observed diffraction intensities are similar to expected intensities based on the structure. Therefore, we infer

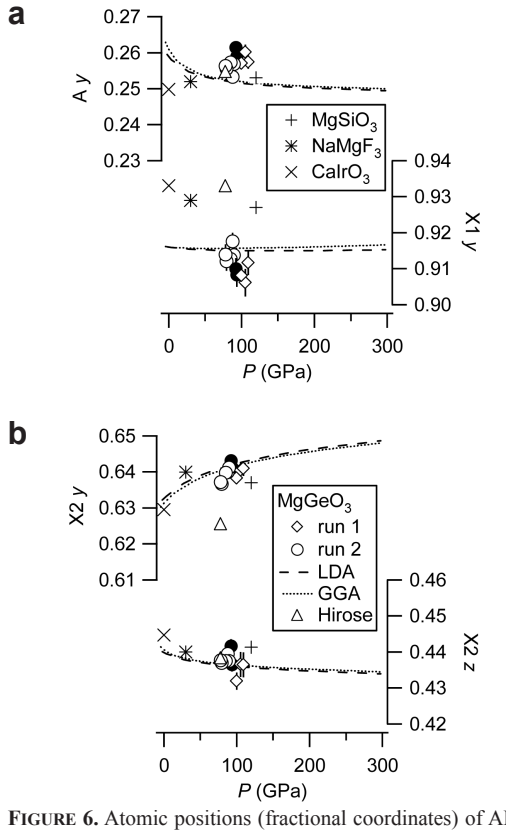

FIGURE 6. Atomic positions (fractional coordinates) of ABX_3 pPv phase. X1 and X2 are corner- and edge-shared anions in BX_6 octahedra, respectively. See Figure 4 for definitions of symbols and references.

that Hirose et al.'s sample had a significant degree of preferred orientation, and their atomic positions may be affected by overfitting in the preferred orientation correction. Overall, the A position in these ABX_3 pPv phases is similar, but X positions are generally different. In particular, O1 *y* position in $MgGeO_3$ is remarkably smaller than those in $MgSiO_3$, $NaMgF_3$, and $CaIrO_3$. It is noted that all the atomic positions in $MgSiO_3$ are very close to those in $NaMgF_3$.

Interatomic distances

$CaIrO_3$-type ABX_3 pPv phase has two coordination polyhedra in its structure, namely AX_8 bicapped trigonal prism (hendecahedron) and BX_6 octahedron (Fig. 1) (Ijjaali et al. 2004). The BX_6 octahedra share X1 corners along the **c**-axis and X2-X2 edges along the **a** axis to form an infinite sheet. The AX_8 hendecahedra share both faces on trigonal prisms in **b-c** plane and edges on pyramid caps to form a layer that separates the sheets of BX_6 octahedra. Figure 7a shows averaged lengths of A-X and B-X bonds in AX_8 hendecahedron and BX_6 octahedron, respectively. Averaged distances of Mg-O in $MgSiO_3$ perovskite up to 12.6 GPa (Ross and Hazen 1990) and Ge-O in $CaGeO_3$ perovskite at room pressure (Sasaki et al. 1983) determined by single-crystal X-ray diffraction at room temperature are compared in this figure. Also shown are Rietveld results of averaged Mg-O distance in $MgSiO_3$ perovskite at 79.7 GPa and 1681 K (Fiquet et al. 2000) and averaged Ge-O distances in α-PbO_2 type GeO_2 at room temperature at 60 GPa (Prakapenka et al. 2003) and 70.7 GPa (Shiraki et al. 2003). Here all Mg and Ge atoms have coordination number of 8 and 6, respectively. Since LDA and GGA results for lattice parameters and atomic positions are consistent, we show only LDA results in figures hereafter for clarity. Theory predicts averaged Mg-O and Ge-O lengths that are in excellent agreement with experimental results using single crystals, validating reliability of theoretical results at low pressures. Previous Rietveld results for averaged Mg-O and Ge-O lengths are also in good agreement with theoretical results, which also support reliability of theoretical results at high pressures. Due to large uncertainty in Rietveld refinement results at high temperature, however, it is difficult to discuss thermal expansion of bond lengths from Rietveld results. The average Mg-O bond length in $MgSiO_3$ pPv is 0.9% smaller than that in $MgGeO_3$ pPv at 120 GPa. Ratio of average bond lengths A-X/B-X in ABX_3 pPv is 1.13 for $MgGeO_3$, 1.17 for $MgSiO_3$, 1.16 for $NaMgF_3$, and 1.21 for $CaIrO_3$.

Figure 7b shows individual bond lengths in the pPv phase. Our Rietveld results from run 1 and run 2 are consistent within uncertainty, and they are also consistent with our theoretical results. Theory predicts enhanced compressibility of Mg-O2 (×4) bond between 0 and ~50 GPa, which is closely related to rapid change of Mg *y* and O2 positions predicted between 0 and ~50 GPa (Fig. 6a). This implies a change of the compression behavior in MgO_8 hendecahedral layer around 50 GPa, which might induce both unusual volume expansion below ~45 GPa and breakdown of the pPv phase below 7 GPa during decompression reported by Kubo et al. (2006). At high temperatures, it is likely that both Ge-O1 and Ge-O2 expand in the GeO_6 octahedron, while Mg-O2(4) is the only bond in MgO_8 hendecahedron that shows evidence for thermal expansion. In $MgSiO_3$, $MgGeO_3$, $NaMgF_3$, and $CaIrO_3$ pPv phases, bond lengths relationships are always B-X1 < B-X2 and A-X1 < A-X2 (×4) < A-X2 (×2).

Distances of seven different neighboring X-X anions in ABX_3 pPv phases are shown in Supplementary Figure 2[1]. Rietveld results, which are generally consistent with theoretical predictions, show that compressibilities of O-O pairs in MgO_8 hendecahedron are generally greater than those in GeO_6 octahedron. The most incompressible O-O pair locates in octahedron (X2-X2_o in Supplementary Fig. 2), while the most compressible pair locates in hendecahedron (both X2-X2_h2 and X1-X2_h in Supplementary Fig. 2). Theoretical calculations showed that compressibilities of O-O pairs in hendecahedron are significantly different from each other compared with those in octahedron. The O2-O2 pair that aligns in the **c**-direction (X2-X2_h1 in Supplementary Fig. 2) is one of the closest O-O pairs, while the O2-O2 pair that aligns in the **a**-direction (X2-X2_oh in Supplementary Fig. 2) is one of the longest O-O pairs in both $MgGeO_3$ and $MgSiO_3$ pPv. These facts may explain the reason for the less axial compressibility of the **c**-axis than the **a**-axis in both $MgGeO_3$ and $MgSiO_3$ pPv (Kubo et al. 2006; Guignot et al. 2007) due to expected higher O-O repulsion in **c**-direction.

Polyhedral volumes

Figure 8a shows the volume change of GeO_6 octahedron and MgO_8 hendecahedron as a function of pressure and temperature. Polyhedral volumes can be calculated from unit-cell volume V_{cell} and the atomic positions using the following equations: $V_{GeO_6} = (8 \times O2\ z \times O1\ y - 8 \times O2\ z - 4 \times O1\ y + 2 \times O2\ y + 3)$

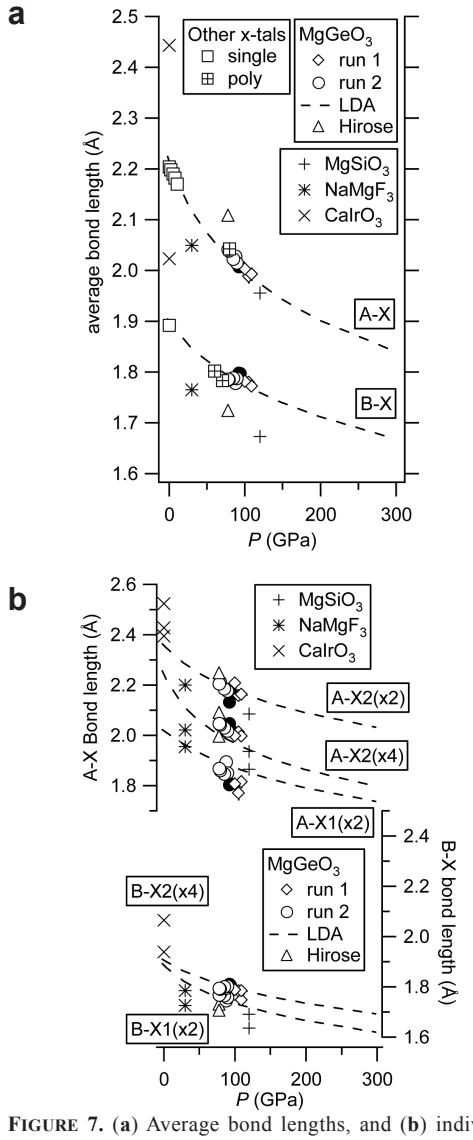

FIGURE 7. (**a**) Average bond lengths, and (**b**) individual bond lengths. Single-crystal results are by Ross and Hazen (1990) for $MgSiO_3$ perovskite up to 12.6 GPa and by Sasaki et al. (1983) for $CaGeO_3$ perovskite at room pressure. Rietveld results are by Fiquet et al. (2000) for $MgSiO_3$ perovskite at 79.7 GPa and 1681 K, and by Prakapenka et al. (2003) and Shiraki et al. (2003) for α-PbO_2 type GeO_2 at room temperature at 60 and 70.7 GPa, respectively. See Figure 4 for the other references.

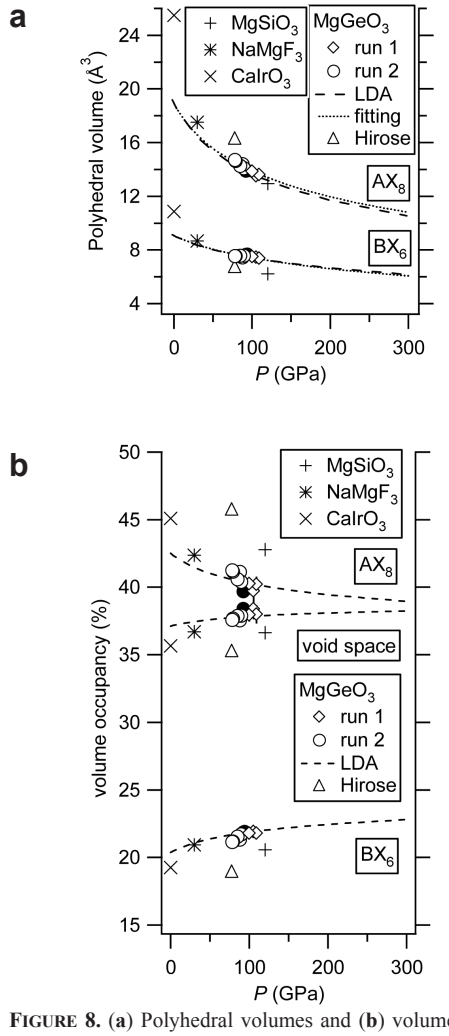

FIGURE 8. (**a**) Polyhedral volumes and (**b**) volume occupancy of polyhedra and void space in ABX_3 pPv phase. Results for the second-order Birch-Murnaghan equation of state fitting using Rietveld results are shown with dotted lines in **a**. See Figure 4 for references.

× V_{cell}/6, and V_{MgO_8} = (–4 × O2 z × O1 y + 12 × O2 z + 5 × O1 y – O2 y – 12 × O_2 y × O2 z – 3) × V_{cell}/12. It is noted that due to existence of void spaces in the crystal structure (Fig. 1a), the unit-cell volume of the pPv phase is given by $4V_{GeO_6} + 4V_{MgO_8} + V_{void}$. Our Rietveld results are in agreement with our theoretical prediction within 2σ.

Theory predicts the following polyhedral compression parameters at 0 K based on third-order Birch-Murnaghan equation of state: polyhedral bulk modulus of 161 GPa for MgO_8 and 301 GPa for GeO_6, pressure derivative of 3.94 for MgO_8 and 4.91 for GeO_6, and zero-pressure polyhedral volume of 18.919 Å^3 for MgO_8 and 9.069 Å^3 for GeO_6. Rietveld results yield the following parameters at room temperature based on second-order Birch-Murnaghan equation of state: polyhedral bulk modulus of 174(3) GPa for MgO_8 and 333(11) GPa for GeO_6, with fixed zero-pressure polyhedral volume of 18.919 Å^3 for MgO_8 and 9.069 Å^3 for GeO_6. As shown here, polyhedral bulk modulus for GeO_6 is 1.9× larger than that for MgO_8. The compression curves fitted to the Rietveld data are also shown in Figure 8a. It is noted that polyhedral volume of MgO_8 in $MgSiO_3$ pPv is similar to that in $MgGeO_3$ despite significant difference of octahedral volume between these two pPv phases.

Figure 8b shows volume occupancy of MgO_8 hendecahedra, GeO_6 octahedra, and void space. Both Rietveld results and theoretical prediction are consistent with each other within 3σ, indicating that volume proportion of the MgO_8 hendecahedral layer significantly decreases with pressure. We do not find any temperature dependence of volume ratio of MgO_8 and GeO_6 polyhedra within uncertainty, implying similar thermal expansivity for MgO_8 and GeO_6 polyhedral layers. Polyhedral volume ratio (V_{AX8}/V_{BX6}) is 1.89 for $MgGeO_3$, 2.08 for $MgSiO_3$,

2.02 for $NaMgF_3$, and 2.34 for $CaIrO_3$. Volume occupancy of the void space is insensitive to pressure, and is similar among the pPv phases.

Octahedral tilting and distortion

The pPv phase has fewer degrees of freedom than the perovskite phase in terms of both tilting and distortion of the octahedra. Because the octahedra in the perovskite phase share corners along all directions, both tilting and symmetrical distortion of octahedra are allowed in all the directions. On the other hand, since the octahedra in the pPv phase share X2-X2 edges along the **a**-axis and share corners in **c**-direction (Fig. 1), tilting of octahedra is allowed only around the **a**-axis, and the X2-X2-X2-X2 plane in an octahedron must have a square or rectangular shape (Fig. 1). Therefore, the shape of octahedral layer in ABX_3 pPv phase can be fully described by specifying both tilting of octahedra around the **a**-axis (B-X1-B angle in **b-c** plane) and the distortion of an octahedron that can be fully described by following three variables: X2-B-X2 angle that represents the deviation of the X2-X2-X2-X2 plane from square to rectangular shape, the angle between X2-X2-X2-X2 plane normal and the B-X1 vector in the **b-c** plane (angle q), and B-X1/B-X2 lengths ratio (Fig. 1). For an ideal octahedron these three variables are 90°, 0°, and 1°, respectively.

As shown below, Rietveld results at 78–109 GPa are consistent with theoretical predictions within 3σ, but considerable data scatter and the limited pressure and temperature range make it difficult to constrain the pressure and temperature dependencies of octahedral tilting and distortion solely from Rietveld results. Therefore, we use theoretical results to compare octahedral tilting and distortion in $MgGeO_3$, $MgSiO_3$, $NaMgF_3$, and $CaIrO_3$ pPv phases.

Tilting of octahedra. Figure 9 shows B-X1-B angle in the **b-c** plane. Theoretical results show a subtle monotonic increase of this angle from 131.3 to 132.7° at 0–300 GPa, indicating that octahedral tilting is insensitive to pressure. Octahedral tilting is ~132° for $MgGeO_3$, ~138° for $MgSiO_3$, and ~140° for both $NaMgF_3$ and $CaIrO_3$, indicating a greater degree of bending in the connection of octahedra in $MgGeO_3$ than the other pPv. The order of octahedral tilting among these pPv can be qualitatively understood by polyhedral volume ratio V_{AX8}/V_{BX6}: A larger (smaller) octahedral tilting makes the length of octahedral layer in **c**-direction shorter (longer). Since $MgGeO_3$ ($CaIrO_3$) has the smallest (largest) V_{AX8}/V_{BX6} among these pPv, octahedra in $MgGeO_3$ ($CaIrO_3$) need to be more (less) bent than the other pPv to share the **a-c** plane with the relatively small (large) hendecahedral layer.

Octahedral distortion. At first, we survey the overall octahedral distortion using angular variance (Fig. 10a), which has been used to show variations in bond angle in an octahedron (Robinson et al. 1971). A regular octahedron has a value of $0°^2$. Theoretical results show a mild decrease of angular variance from 12 to $6°^2$ by compression from 50 to 300 GPa, predicting that basic evolution of angular variance with pressure is to decrease distortion over a wide pressure range. However, the pressure change of angular variance is somewhat larger below 50 GPa (from 12 to $18°^2$ by decompression to 0 GPa), consistent with different compression behavior below 50 GPa. Angular variance of the pPv phase is greater than that of $MgSiO_3$ perovskite phase ($1.7°^2$ at ambient conditions by Ross and Hazen 1990; $2.4°^2$ at 79.7 GPa, 1681 K by Fiquet et al. 2000), and is ~$11°^2$ for $MgGeO_3$, ~$7°^2$ for both $MgSiO_3$ and $NaMgF_3$, and ~$38°^2$ for $CaIrO_3$, showing that $MgSiO_3$, $MgGeO_3$, and $NaMgF_3$ are similarly less distorted than $CaIrO_3$.

Figure 10b shows X2-B-X2 angle in a BX_6 octahedron. We define this angle so that the X2-X2 vector is parallel to the **a**-direction. Theoretical calculations predict a modest decrease of this angle with pressure, which contributes to decrease of octahedral distortion with pressure. Results from Rietveld refinements are consistent with theory within 3σ, but Rietveld results also imply that this angle may change more than predicted (~92° at 90 GPa to ~94° at 80 GPa during decompression). Since faster increase of this angle during decompression can result in rapid expansion of **a**-axis, we speculate that the greater change of this angle with pressure may explain the anomaly in b/a ratio reported by Kubo et al. (2006). This angle is 92.1° in $MgGeO_3$, 93.4° in $MgSiO_3$, 94.4° in $NaMgF_3$, and 99.2° in $CaIrO_3$, showing significant distortion of $CaIrO_3$. The order of this angle among these pPv can be qualitatively understood by considering the V_{AO8}/V_{BO6} polyhedral volume ratio following the same logic put forward in the discussion of the octahedral tilting among these pPv.

Figure 10c shows pressure dependence of the angle between X2-X2-X2-X2 plane normal and B-X1 vector in **b-c** plane (angle q). Theory predicts slight monotonic decrease of this angle by compression, which also contributes to decrease of octahedral distortion with pressure. This angle is ~3° in $MgSiO_3$, ~1° in $NaMgF_3$, and ~5° in both $MgGeO_3$ pPv and $CaIrO_3$, showing that $NaMgF_3$ is least distorted.

Figure 10d shows the ratio of B-X1 and B-X2 lengths. Theory predicts deviation of this ratio from 1 with pressure with relatively rapid change below 50 GPa and relatively mild change above 50 GPa, contributing to an increase of octahedral distortion with pressure. This ratio is 0.971 in $MgGeO_3$, 0.967 in both $MgSiO_3$ and $NaMgF_3$, and 0.939 in $CaIrO_3$, showing that $MgSiO_3$, $NaMgF_3$, and $MgGeO_3$ are similarly less distorted than $CaIrO_3$.

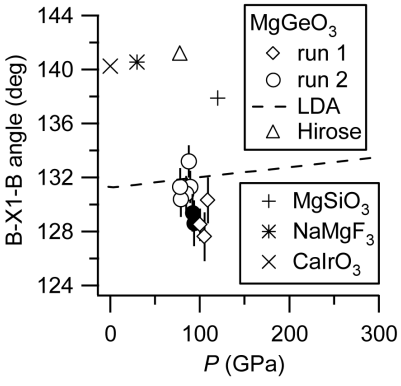

FIGURE 9. Tilting angle of octahedra around the **a**-axis (= B-X1-B angle between two octahedra in **b-c** plane) in ABX_3 pPv phase. See Figure 4 for references.

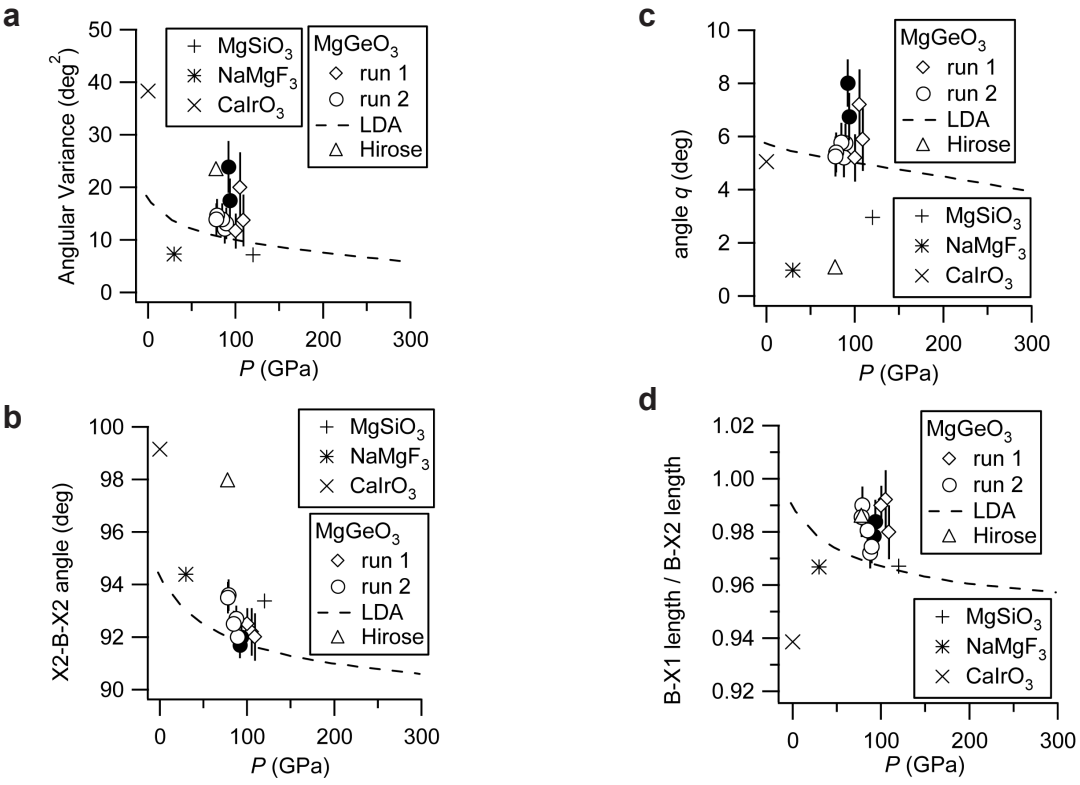

FIGURE 10. Distortion parameters for BX_6 octahedron in ABX_3 pPv phase. (**a**) Angular variance, (**b**) X2-B-X2 angle (where X2-X2 vector is parallel to *a* direction), (**c**) angle *q* (the angle between X2-X2-X2-X2 plane normal and B-X1 vector in *b*-*c* plane), and (**d**) B-X1/B-X2 lengths ratio. X1 and X2 are corner- and edge-shared oxygen in BX_6 octahedra, respectively. See Figure 4 for references.

Comparison of $MgGeO_3$, $MgSiO_3$, $NaMgF_3$, and $CaIrO_3$ pPv

There are some similarities between $MgSiO_3$ and $MgGeO_3$ pPv represented by axial ratios, averaged Mg-O distance, MgO_8 polyhedral volume, and degree of octahedral distortion as well as consistency in elastic systematics and generally similar behavior in axial compressibilities reported by Kubo et al. (2006). On the other hand, $NaMgF_3$ pPv phase shows more similarities in structural parameters with $MgSiO_3$ pPv than $MgGeO_3$ pPv, while the similarity between $MgSiO_3$ and $CaIrO_3$ pPv is limited to octahedral tilt angle. Therefore, we infer that $NaMgF_3$ may be a good analog material to $MgSiO_3$ pPv, and among oxide pPv, $MgGeO_3$ is a better analog than $CaIrO_3$. It is noted that Lindsay-Scott et al. (2007) have also inferred that $CaIrO_3$ may not be a good analog for $MgSiO_3$ pPv based on comparison of axial incompressibility ratios for $CaIrO_3$ and $MgSiO_3$ pPv. It should also be noted that $MgGeO_3$ and $CaIrO_3$ pPv phases tend to show qualitatively opposite character with the relationship to $MgSiO_3$ pPv phase, such as axial ratios, atomic positions, ratio of average bond lengths (A-O/B-O), variation of bond lengths in AO_8 and BO_6 polyhedra (Fig. 7b), polyhedral volume ratio, and octahedral tilting angle. This implies that physical properties of $MgSiO_3$ pPv (such as elasticity and rheology) might be intermediate between the properties of the two analog materials.

Reliability of Rietveld refinements to Mbar pressures

Many previous high-pressure studies report only a single optimum Rietveld refinement and this leaves open significant questions about the robustness of the reported results. In addition, there is a large disagreement between the Rietveld results reported here and that of Hirose et al. (2005) on the same material at similar conditions. The existence of such discrepancies, despite each providing an overall reasonable fit to the diffraction data, could raise questions about the reliability of the Rietveld method at extreme conditions.

The present results show that we can obtain consistent Rietveld refinements for experiments involving separate samples with different pressure transmitting media that cover a similar pressure range. Furthermore, these refinement results are in good agreement with our independent first-principles calculations. Consistent results are also obtained for individual and averaged bond lengths between theory and experiment. Finally, the averaged Mg-O and Ge-O bond lengths found here are consistent with previous experimental studies (single-crystal and polycrystalline) of other materials with similar structural elements at high pressures. These consistencies all suggest that Rietveld refinement can provide reasonable structural parameters at pressures approaching 1 Mbar.

ACKNOWLEDGMENTS

This work was supported by NSF and the Carnegie-DOE Alliance Center. A.K. benefited greatly from the powder X-ray diffraction workshop held at National Synchrotron Light Source in January 2005 organized by John Parise, Peter Stephens, and Patrick Woodward. We thank Robert J. Cava for his help with sample synthesis and Sean R. Shieh for experimental assistance. Preliminary experiments were conducted at HPCAT, APS, Argonne National Laboratory with the help of Yue Meng. Comments by Leonid Dubrovinsky and anonymous reviewers improved the manuscript. Discussions with Haozhe Liu and Przemyslaw Dera were also helpful. This work was performed at GSECARS, APS, Argonne National

Laboratory. GSECARS is supported by the NSF, Earth Sciences (EAR-0622171) and DOE-Geosciences (DE-FG02-94ER14466). Use of the Advanced Photon Source is supported by DOE Office of Basic Energy Sciences under contract no. DE-AC02-06CH11357.

REFERENCES CITED

Blöchl, P.E. (1994) Projector augmented-wave method. Physical Review B, 50, 17953–17979.

Fang, C.M. and Ahuja, R. (2006) Structures and stability of ABO_3 orthorhombic perovskites at the Earth's mantle conditions from first-principles theory. Physics of the Earth and Planetary Interiors, 157, 1–7.

Fiquet, G., Dewaele, A., Andrault, D., Kunz, M., and LeBihan, T. (2000) Thermoelastic properties and crystal structure of $MgSiO_3$ perovskite at lower mantle pressure and temperature conditions. Geophysical Research Letters, 27, 21–24.

Fiquet, G., Guyot, F., Kunz, M., Matas, J., Andrault, D., and Hanfland, M. (2002) Structural refinements of magnesite at very high pressure. American Mineralogist, 87, 1261–1265.

Guignot, N., Andrault, D., Morard, G., Bolfan-Casanova, N., and Mezouar, M. (2007) Thermoelastic properties of post-perovskite phase $MgSiO_3$ determined experimentally at core-mantle boundary *P-T* conditions. Earth and Planetary Science Letters, 256, 162–168.

Hammersley, A.P., Svensson, S.O., Hanfland, M., Fitch, A.N., and Häusermann, D. (1996) Two-dimensional detector software: From real detector to idealized image or two-theta scan. High Pressure Research, 14, 235–248.

Hirose, K. (2006) Postperovskite phase transition and its geophysical implications. Reviews of Geophysics, 44, RG3001.

Hirose, K. and Fujita, Y. (2005) Clapeyron slope of the post-perovskite phase transition in $CaIrO_3$. Geophysical Research Letters, 32, L13313.

Hirose, K., Kawamura, K., Ohishi, Y., Tateno, S., and Sata, N. (2005) Stability and equation of state of $MgGeO_3$ post-perovskite phase. American Mineralogist, 90, 262–265.

Hohenberg, P. and Kohn, W. (1964) Inhomogeneous electron gas. Physical Review, 136, B864–B871.

Holmes, N.C., Moriarty, J.A., Gathers, G.R., and Nellis, W.J. (1989) The equation of state of platinum to 660 GPa (6.6 Mbar). Journal of Applied Physics, 66, 2962–2967.

Ibers, J.A., Templeton, D.H., Vainshtein, B.K., Bacon, G.E., and Lonsdale, K. (1968) International Tables for X-ray Crystallography, Vol. III, p. 233–244. Kynoch Press, Birmingham.

Iitaka, T., Hirose, K., Kawamura, K., and Murakami, M. (2004) The elasticity of the $MgSiO_3$ post-perovskite phase in the Earth's lowermost mantle. Nature, 430, 442–445.

Ijjaali, I., Mitchell, K., Huang, F.Q., and Ibers, J.A. (2004) Syntheses and characterization of the actinide manganese selenides $ThMnSe_3$ and $UMnSe_3$. Journal of Solid State Chemistry, 177, 257–261.

Kavner, A. and Duffy, T.S. (2003) Elasticity and rheology of platinum under high pressure and nonhydrostatic stress. Physical Review B, 68, 144101.

Kohn, W. and Sham, L.J. (1965) Self-consistent equations including exchange and correlation effects. Physical Review, 140, 1133–1138.

Kojitani, H., Furukawa, A., and Akaogi, M. (2007) Thermochemistry and high-pressure equilibria of the post-perovskite phase transition in $CaIrO_3$. American Mineralogist, 92, 229–232.

Kresse, G. and Furthmüller, J. (1996) Efficient iterative schemes for ab initio total-energy calculations using a plane-wave basis set. Physical Review B, 54, 11169–11186.

Kresse, G. and Hafner, J. (1993) Ab initio molecular dynamics for liquid metals. Physical Review B, 47, 558–561.

——— (1994) Ab initio molecular-dynamics simulation of the liquid-metal-amorphous-semiconductor transition in germanium. Physical Review B, 49, 14251–14269.

Kresse, G. and Joubert, D. (1999) From ultrasoft pseudopotentials to the projector augmented-wave method. Physical Review B, 59, 1758–1775.

Kubo, A., Kiefer, B., Shen, G., Prakapenka, V.B., Cava, R.J., and Duffy, T.S. (2006) Stability and equation of state of the post-perovskite phase in $MgGeO_3$ to 2 Mbar. Geophysical Research Letters, 33, L12S12.

Larson, A.C. and Von Dreele, R.B. (2004) General Structure Analysis System (GSAS). Los Alamos National Laboratory Report LAUR 86–748.

Lindsay-Scott, A., Wood, I.G., and Dobson, D.P. (2007) Thermal expansion of $CaIrO_3$ determined by X-ray powder diffraction. Physics of the Earth and Planetary Interiors, 162, 140–148.

Liu, H.Z., Chen, J., Hu, J., Martin, C.D., Weidner, D.J., Häusermann, D., and Mao, H.K. (2005) Octahedral tilting evolution and phase transition in orthorhombic $NaMgF_3$ perovskite under pressure. Geophysical Research Letters, 32, L04304.

Mao, W.L., Shen, G., Prakapenka, V.B., Meng, Y., Campbell, A.J., Heinz, D.L., Shu, J., Hemley, R.J., and Mao H.K. (2004) Ferromagnesian postperovskite silicates in the D" layer of the Earth. Proceedings of the National Academy of Sciences of the United States of America, 101, 15867–15869.

Martin, C.D., Crichton, W.A., Liu, H., Prakapenka, V., Chen, J., and Parise, J.B. (2006a) Rietveld structure refinement of perovskite and post-perovskite phases of $NaMgF_3$ (neighborite) at high pressures. American Mineralogist, 91, 1703–1706.

——— (2006b) Phase transitions and compressibility of $NaMgF_3$ (neighborite) in perovskite- and post-perovskite-related structures. Geophysical Research Letters, 33, L11305.

Martin, C.D., Meng, Y., Prakapenka, V., and Parise, J.B. (2008) Gasketing optimized for large volume in the diamond anvil cell: first application to $MgGeO_3$ and implications for structural systematics of the perovskite to post-perovskite transition. Journal of Applied Crystallography, 41, 38–43.

McCusker, L.B., Von Dreele, R.B., Cox, D.E., Louër, D., and Scardi, P. (1999) Rietveld refinement guidelines. Journal of Applied Crystallography, 32, 36–50.

Merkel, S., Kubo, A., Miyagi, L., Speziale, S., Duffy, T.S., Mao, H.K., and Wenk, H.-R. (2006) Plastic deformation of $MgGeO_3$ post-perovskite at lower mantle pressure. Science, 311, 644–646.

Merkel, S., McNamara, A.K., Kubo, A., Speziale, S., Miyagi, L., Meng, Y., Duffy, T.S., and Wenk, H.-R. (2007) Deformation of $(Mg,Fe)SiO_3$ post-perovskite and D" anisotropy. Science, 316, 1729–1732.

Miyagi, L., Nishiyama, N., Wang, Y., Kubo, A., West, D.V., Cava, R.J., Duffy, T.S., and Wenk, H.-R. (2008) Deformation and texture development in $CaIrO_3$ post-perovskite phase up to 6 GPa and 1300 K. Earth and Planetary Science Letters, 268, 515–525.

Murakami, M., Hirose, K., Kawamura, K., Sata, N., and Ohishi, Y. (2004) Post-perovskite phase transition in $MgSiO_3$. Science, 304, 855–858.

Oganov, A.R. and Ono, S. (2004), Theoretical and experimental evidence for a post-perovskite phase of $MgSiO_3$ in Earth's D" layer. Nature, 430, 445–448.

Oganov, A.R., Martoňák R., Laio A., Raiteri, P., and Parrinello, M. (2005), Anisotropy of Earth's D" layer and stacking faults in the $MgSiO_3$ post-perovskite phase. Nature, 438, 1142–1144.

Ono, S. and Oganov, A.R. (2006) In situ observations of phase transition between perovskite and $CaIrO_3$-type phase in $MgSiO_3$ and pyrolitic mantle composition. Earth and Planetary Science Letters, 236, 914–932.

Ono, S. and Ohishi, Y. (2005) In situ X-ray observation of phase transformation in Fe_2O_3 at high pressures and high temperatures. Journal of Physics and Chemistry of Solids, 66, 1714–1720.

Ono, S., Oganov, A.R., Koyama, T., and Shimizu, H. (2006a) Stability and compressibility of the high-pressure phase of Al_2O_3 up to 200 GPa: Implications for the electrical conductivity of the base of the lower mantle. Earth and Planetary Science Letters, 246, 326–335.

Ono, S., Kikegawa, T., and Ohishi, Y. (2006b) Equation of state of $CaIrO_3$-type $MgSiO_3$ up to 144 GPa. American Mineralogist, 91, 475–478.

Ozima, M. and Akimoto, S.-I. (1983) Flux growth of single crystals of $MgGeO_3$ polymorphs (orthopyroxene, clinopyroxene, and ilmenite) and their phase relations and crystal structures. American Mineralogist, 68, 1199–1205.

Perdew, J.P. and Zunger, A. (1981) Self-interaction correction to density-functional approximations for many-electron systems. Physical Review B, 23, 5048–5079.

Perdew, J.P., Burke, K., and Ernzerhof, M. (1996) Generalized gradient approximation made simple. Physical Review Letters, 77, 3865–3868.

Prakapenka, V.B., Dubrovinsky, L.S., Shen, G., Rivers. M.L., Sutton, S.R., Dmitriev, V., Weber, H.-P., and Le Bihan, T. (2003) α-PbO_2-type high-pressure polymorph of GeO_2. Physical Review B, 67, 132101.

Robinson, K., Gibbs, G.V., and Ribbe, P.H. (1971) Quadratic elongation: A quantitative measure of distortion in coordination polyhedra. Science, 172, 567–570.

Rodi, V.F. and Babel, D. (1965) Erdalkaliiridium(IV)-oxide: Kristallstruktur von $CaIrO_3$. Zeitschrift für anorganische und allgemeine Chemie, 336, 17–23.

Ross, N.L. and Hazen, R.M. (1990) High-pressure crystal chemistry of $MgSiO_3$ perovskite. Physics and Chemistry of Minerals, 17, 228–237.

Runge, C.E., Kubo, A., Kiefer, B., Meng, Y., Prakapenka, V.B., Shen, G., Cava, R.J., and Duffy, T.S. (2006) Equation of state of $MgGeO_3$ perovskite to 65 GPa: Comparison with the post-perovskite phase. Physics and Chemistry of Minerals, 33, 699–709.

Santillán, J., Shim, S.H., Shen, G., and Prakepanka, V.B. (2006) High-pressure phase transition in Mn_2O_3: Application for the crystal structure and preferred orientation of the $CaIrO_3$ type. Geophysical Research Letters, 33, L15307.

Sasaki, S., Prewitt, C.T., and Liebermann, R.C. (1983) The crystal structure of $CaGeO_3$ perovskite and the crystal chemistry of the $GeFeO_3$-type perovskites. American Mineralogist, 68, 1189–1198.

Shen, G., Rivers, M.L., Wang, Y., and Sutton, S.R. (2001) Laser heated diamond cell system at the Advanced Photon Source for in situ X-ray measurements at high pressure and temperature. Reviews of Scientific Instruments, 72, 1273–1282.

Shen, G., Prakapenka, V.B., Eng, P.J., Rivers, M.L., and Sutton, S.R. (2005) Facilities for high-pressure research with the diamond anvil cell at GSECARS. Journal of Synchrotron Radiation, 12, 642–649.

Shieh, S.R., Duffy, T.S., Kubo, A., Shen, G., Prakapenka, V.B., Sata, N., Hirose, K.,

and Ohishi, Y. (2006) Equation of state of the post-perovskite phase synthesized from a natural (Mg,Fe)SiO_3 orthopyroxene. Proceedings of the National Academy of Sciences of the United States of America, 103, 3039–3043.
Shim, S.-H., Duffy, T.S., Jeanloz, T., and Shen, G. (2004) Stability and crystal structure of $MgSiO_3$ perovskite to the core-mantle boundary. Geophysical Research Letters, 31, L10603.
Shim, S.-H., Kubo, A., and Duffy, T.S. (2007) Raman spectroscopy of perovskite and post-perovskite phases of $MgGeO_3$ to 123 GPa. Earth and Planetary Science Letters, 260, 166–178.
Shiraki, K., Tsuchiya, T., and Ono, S. (2003) Structural refinements of high-pressure phases in germanium dioxide. Acta Crystallographica, B59, 701–708.
Singh, A.K. (1993) The lattice strains in a specimen (cubic system) compressed nonhydrostatically in an opposed anvil device. Journal of Applied Physics, 73, 4278–4286.
Sugahara, M., Yoshiasa, A., Komatsu, Y., Yamanaka, T., Bolfan-Casanova, N., Nakatsuka, A., Sasaki, S., and Tanaka, M. (2006) Reinvestigation of the $MgSiO_3$ perovskite structure at high pressure. American Mineralogist, 91, 533–536.
Tateno, S., Hirose, K., Sata, N., and Ohishi, Y. (2006) High-pressure behavior of $MnGeO_3$ and $CdGeO_3$ perovskites and the post-perovskite phase transition. Physics and Chemistry of Minerals, 32, 721–725.
Toby, B.H. (2001) EXPGUI, a graphical user interface for GSAS. Journal of Applied Crystallography, 34, 210–213.
——— (2006) *R* factors in Rietveld analysis: How good is good enough? Powder Diffraction, 21, 67–70.
Tsuchiya, T., Tsuchiya, J., Umemoto, K., and Wentzcovitch, R.M. (2004) Phase transition in $MgSiO_3$ perovskite in the Earth's lower mantle. Earth and Planetary Science Letters, 224, 241–248.
Umemoto, K., Wentzcovitch, R.M., Weidner, D.J., and Parise, J.B. (2006) $NaMgF_3$: A low-pressure analog of $MgSiO_3$. Geophysical Research Letters, 33, L15304.
Von Dreele, R.B. (1997) Quantitative texture analysis by Rietveld refinement. Journal of Applied Crystallography, 30, 517–525.
Walte, N., Heidelbach, F., Miyajima, N., and Frost, D. (2007) Texture development and TEM analysis of deformed $CaIrO_3$: Implications for the D'' layer at the core-mantle boundary, Geophysical Research Letters, 34, L08306.
Wentzcovitch, R.M., Tsuchiya, T., and Tsuchiya, J. (2006) $MgSiO_3$ postperovskite at D" conditions. Proceedings of the National Academy of Sciences of the United States of America, 103, 543–546.

Manuscript received May 9, 2007
Manuscript accepted January 30, 2008
Manuscript handled by Artem Oganov

Note added in Proof

Martin et al. (2008) also recently reported structure refinements of $MgGeO_3$ post-perovskite at 84–89 GPa.